- SUPPLEMENTARY INFORMATION -

Garnet xenocryst from petit-spot lavas as an indicator for off-axis mantle refertilization at intermediate spreading ridges.

L. Rochat[1], S. Pilet[1*], O. Müntener[1], T. Duretz[1,2], L. Baumgartner[1], N. Abe[3] & N. Hirano[4]

[1] Institute of Earth Science, University of Lausanne, Switzerland;

[2] Géosciences Rennes, Université de Rennes 1, CNRS UMR 6118, France;

[3] R&D Center for Ocean Drilling Science, Japan Agency for Marine-Earth Science and Technology (JAMSTEC), Yokosuka, Japan;

[4] Center for NE-Asian Studies, Tohoku University, Sendai, Japan.

1. Supplementary Methods

Microprobe mineral analyses

Garnet xenocryst and associated minerals were analyzed using a wavelength-dispersive JEOL 8200 electron microprobe at the Institute of Earth Sciences, University of Lausanne, Switzerland. All analyses were performed using an acceleration voltage of 15 kV, a beam current of 15 nA and a focused beam (1 µm). Si, Al, Ti, Mg, Fe, Mn, Ca, Na, K and Cr were determined and all data were processed using CITZAF (Armstrong, 1988). Synthetic and natural oxides and silicates were used as standards. Several profiles were performed (Figs S1 and S3) to test the homogeneity of the grt xenocrysts. Analyses from profile 4 and mean value are reported in Table S1.

LA-ICP-MS analyses

Concentrations of selected trace elements (REE, HFSE and LILE) in the garnet xenocryst were determined in situ by laser ablation ICP-MS at the Institute of Earth Sciences, University of Lausanne, Switzerland. Analyses were performed on a sector-field ICP-MS single collector spectrometer Element XR interfaced to a NewWave UP-193 ArF excimer ablation system at a pulse repetition rate of 15 Hz. As we have observed garnet xenocryst in only one thin section, we have been constrained to use the EMPA polished thin section (30µm) for the LA-ICP-MS analyses. A large beam size (150 µm of diameter) was used to compensate the limited thickness of the polish section. Acquisition time for the garnet xenocryst was preceded by ~60s background measurement and ~14 to 19s mineral measurement as a function of the thickness of the thin section and the ablation yield.

Calibration and sensitivity of the instrument was performed on the NIST SRM-612 glass standard with linear scan at an energy density of ~4.5 J/cm2, and a repetition rate of 20Hz and 75 µm of diameter. The standard was analyzed two times before and two times after garnet analyses with a diameter of 75 µm. Data reduction was conducted using LamTrace software (Longerich et al., 1996). ^{42}Ca was used as an internal standard that was previously determined by electron microprobe analyses.

2. Supplementary description

The garnet xenocryst (Fig. 1 and Fig. S1) is observed in the thin section KR04-D08-017c of *petit-spot* lava sampled on site B as described by Hirano et al. (2006). The garnet is around 1 mm in size, and shows three distinct parts: a chemically homogeneous core, a symplectite zone and a reaction zone. The fibrous aspect of the garnet xenocryst shown in figure 1 is due to the presence of micro-symplectites in the core (only visible using an electronic microscope at high magnification, x450) that increase in size in the so-called symplectite zone (Fig. S2). Unfortunately, the mineral size in the micro-symplectite zone (>>1 µm) is too small to perform WDS microprobe analysis.

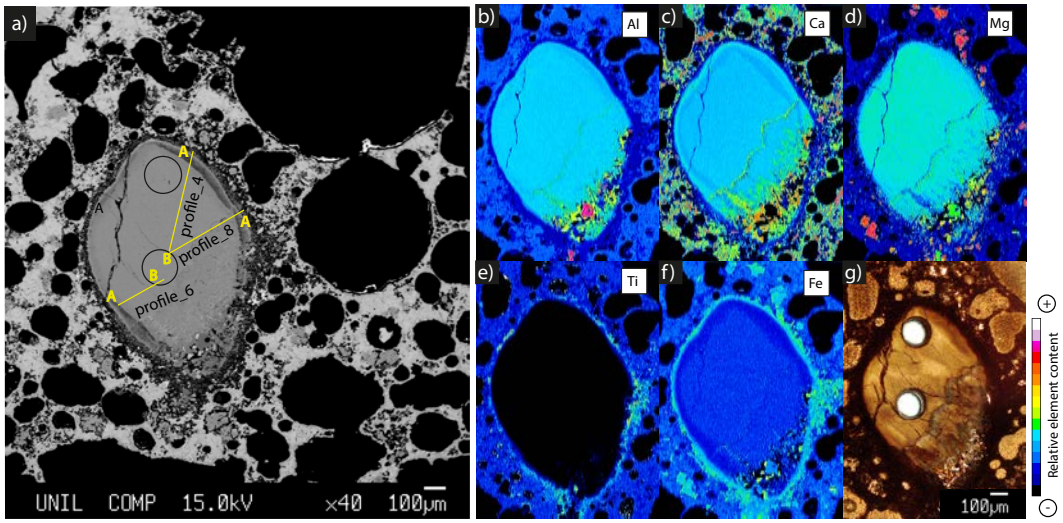

Figure S1: garnet xenocryst from petit-spot lava images. **a**: Back-scattered electron (BSE) image of the garnet xenocryst enclosing in highly vesicular volcanic glass with the location of the three EMPA profiles performed to obtain average composition of this xenocryst. **b-f**: X-ray maps of the garnet xenocryst for Al, Ca, Mg, Ti and Fe respectively. The color scales indicate relative element contents: red colors correspond to higher concentration. **g**: Photomicrograph of the garnet xenocryst obtained after X-ray maps and LA-ICP-MS data acquisition.

A kelyphite rim (80 µm wide) surrounds the crystal (dark brown part around the garnet in Figure S1g). K_2O and Na_2O content are clearly higher in the kelyphite rim compared to the garnet xenocryst core (Fig. S03). For the mean calculation of the garnet core composition (Table S1), the kelyphite rim was excluded on the basis of the Na_2O and K_2O content. Only the part designated as the core in Fig S3 was used for this calculation. X-ray maps (Fig. S01b-f) show an decrease of the Al and Ca content associated with an increase of Fe content in the kelyphite rim. These changes are interpreted as the interaction of the garnet xenocryst with the surrounding *petit-spot* melt during the transport of the xenocryst to the surface. In contrast, the formation of symplectite are interpreted, not as crystal-melt interaction, but associated to the change of P-T conditions.

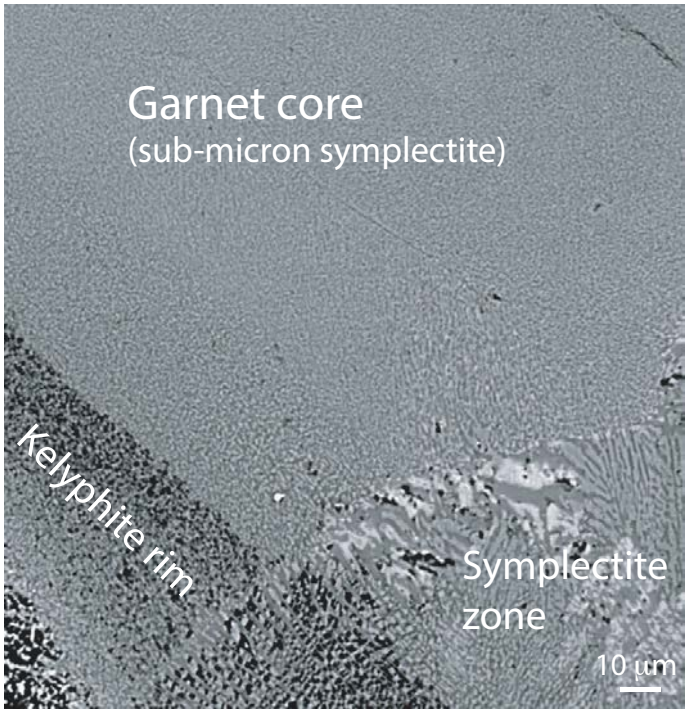

Figure S2: Back-scattered electron (BSE) image of the garnet xenocryst showing the core composed of sub-micron symplectite, the symplectite zone and the kelyphite rim. BSE image was obtained with a magnification of x450.

Electron microprobe analyses and X-ray maps (Table S1 and Fig. S1b-f) indicate that the core is characterized by a homogeneous pyrope-rich composition (Py_{62}, Gr_{20}, Al_{18}; Fig. S04) with low Cr_2O_3 (0.07-0.21 wt. %; Fig. 2) and TiO_2 (0.06-0.17 wt. %) content, and no mineral inclusion. The Al content ranges from 20.9 to 24.7 wt% and MnO content from 0.14 to 0.24 wt%. (Table S1).

The reaction zone (bottom part of the crystal, Fig. S1) is characterized by the association of orthopyroxene (Mg# 79-84), plagioclase (An 85-93), spinel (Cr# 0.39-0.75) and olivine (Fo 78-81). One larger hercynitic spinel (Cr_2O_3: 0.55 wt. %) of around 75 µm in size (significantly larger that other minerals observed in this zone) is also present in the reaction zone. We hypothesize that the reaction zone is produced by the breakdown of garnet at decreasing pressure producing opx + plg+ spl and minor ol.

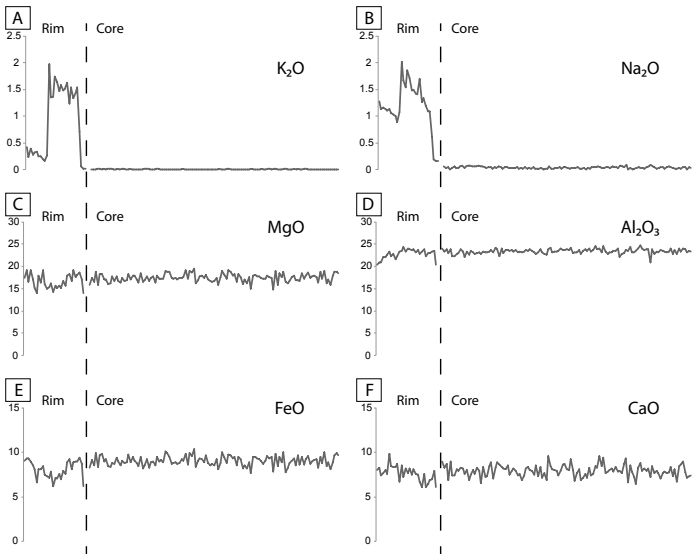

Figure S3: Electron microprobe analysis for major elements in wt. % from the kelyphite rim toward the core (from the left to the right) of the garnet xenocryst (profile 4, see Fig. S1a, for location). **A** and **B** show analyses for K_2O and Na_2O, respectively, where the kelyphite rim is clearly identified with elevated contents of these elements. **C** to **F**: MgO, Al_2O_3, FeO and CaO display relatively homogeneous compositions in the core.

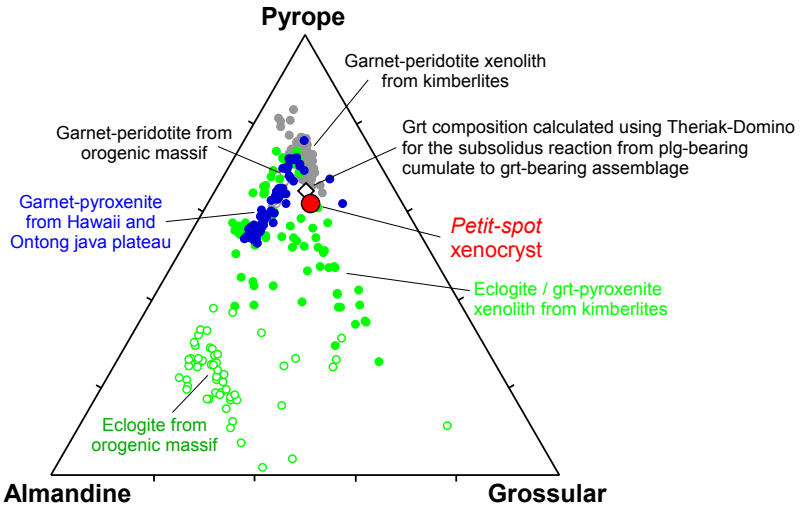

Figure S4: Ternary diagram garnet composition showing the garnet xenocryst from *petit-spot* lava (full red circle) compared to garnet-peridotite xenolith from kimberlites (full grey circles: Ionov et al., 1993, 2010; Canil and O'Neill, 1996; Litasov et al., 2000; van Achterbergh et al., 2001; Gregoire et al., 2003; Simon, 2003; Ziberna et al., 2013), garnet-peridotite from orogenic massif (open grey circles: Beyer et al., 2006; Scambelluri et al., 2014), garnet-pyroxenite from Hawaii and Ontong Java plateau (full blue circles: Ishikawa et al., 2004; Bizimis et al., 2005; Keshav et al., 2007), eclogite / garnet-pyroxenite xenoliths from kimberlites (full green circles: Jacob and Foley, 1999; Schulze et al., 2000; Litasov et al., 2000; Peltonen et al., 2002; Jacob et al., 2003; Smart et al., 2009; Tappe et al., 2011; Pernet-Fisher et al., 2014), eclogites from orogenic massif (open green circles: Evans et al., 1979; Clarke et al., 1997; King et al., 2004; Bucher, 2005)

Trace element composition

Trace element contents of the garnet core were measured two times according to the size of the xenocryst (Fig. S1g). The figure S5 shows similar composition for the 2 analyses except for Rb, Ba, Pb, Ce and La where small differences are observed. The trace element patterns for the garnet xenocryst have depleted highly incompatible element (Rb to La), flat HREE (Sm to Lu) with primitive mantle normalized values around 1 (Table S03). A slight positive Eu anomaly and a slight negative Ti anomaly regarding element with similar degree of incompatibility is also observed. (Fig. S05).

The trace element pattern of garnet xenocrysts share many similarity with the patterns of "eclogitic" garnet analyzed by Jacob et al. (2003), which are interpreted as formed by metamorphic reaction of an initial gabbroic protolith.

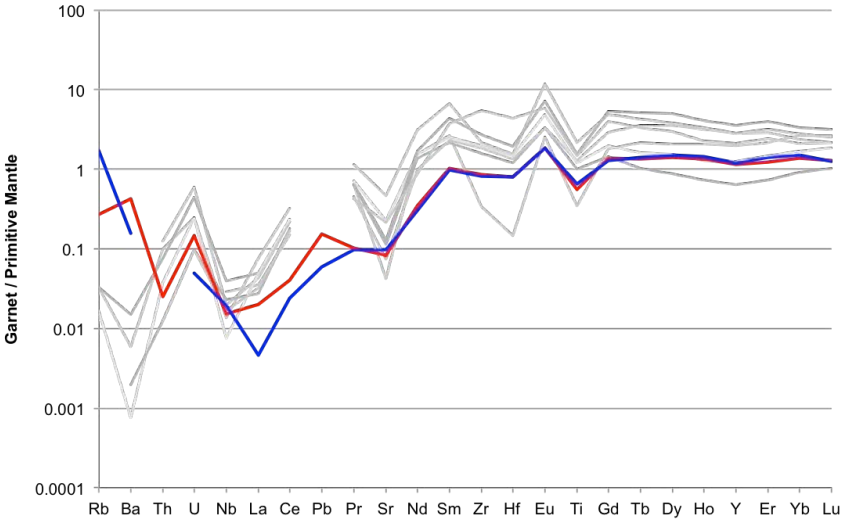

Figure S5: Trace element content normalized to primitive mantle (McDonough and Sun 1995) for the garnet xenocryst from petit-spot lava (see LA-ICP-MS data acquisition method above) compared to "eclogitic" garnet from Jacob et al. (2003)

3. Supplementary discussion

Subsolidus phase relations

In order to evaluate the pressure range at which garnet can be formed from a plagioclase-bearing cumulate, we calculated a P-T diagram (Fig. S06) using Theriak-Domino (de Capitani and Petrakakis, 2010).

Fractional crystallization experiments performed by Villiger *et al.* (2004) at 1 GPa show that differentiation of a primitive tholeiitic basalt produces various cumulates as a function of temperature. We used the cumulate composition SV54 (59% cpx, 8% opx, 28% plg, 5% sp) as input composition for the modeling. This cumulate was crystallized at 1210°C and it was in equilibrium with a slightly differentiated tholeiitic melt (Mg#: 59) composition. This cumulate was selected because it is the first cumulate where plagioclase appears during fractional crystallization at 1.0 GPa, but the effect of this choice was further tested (see below) by using different compositions. The chemical composition of cumulate SV54 (Fig. S6) was calculated from the mineral modes and mineral compositions reported in Villiger et al. (2004). Results are given in molar proportions.

The thermodynamic database used for the calculation is from Berman (1988) with modification of Berman (1990) with solid solutions from Berman and Aranovich (1996) and Aranovich and Berman, (1996) and Meyre et al., (1997)

The P-T diagram reported in figure S6 shows that the transition from a plg-bearing cumulate at high temperature to garnet bearing metamorphic assemblages at lower temperature is possible only in a limited range: from 1200°C at 1.2 GPa to 650°C at 0.7 GPa. Lower temperature for plg-grt transition seems unlikely as low temperature will limit the reaction kinetic / crystal growth. The evolution of phase proportions calculated by Theriak-Domino for the cooling of the gabbroic cumulate from 1200°C to 800°C at 1 GPa is shown in figure S7. This figure illustrates that large proportions of garnet are produced by such a reaction. Moreover, the garnet compositions predicted by thermodynamic calculations ($Mg_{1,62}$,$Fe_{0.77}$,$Ca_{0.61}$) and measured *petit-spot* garnet xenocryst ($Mg_{1,86}$,$Fe_{0.54}$,$Ca_{0.60}$) are in agreement except the Mg#, which is slightly lower in the thermodynamic calculation. This difference can easily be explained by a small over-estimation of the FeO/MgO ratio in the whole rock composition. Alternatively, it could be due to FeO loss and MgO gain

during cooling of >100Ma in the lithospheric mantle between the formation of gabbroic cumulate and the sampling of this garnet xenocrysts by petit-spot lava. To evaluate the sensitivity of the phase diagram to different starting composition, in particular the potential presence of olivine in the cumulate, we performed P-T calculations using various mineral cumulate assemblages reported by Villiger *et al.* (2004) for the fractional crystallization experiments. Figure S8 shows that the location of the plagioclase to garnet subsolidus reaction is not affected significantly for the different assemblages (SV 54: 1210°C; SV57: 1180°C; SV58: 1150°C). In contrast, the addition of 10% of olivine to the initial SV 54 plg, cpx, opx, sp assemblage shifts by up to 1 Kbar. This increase of pressure does not change the conclusions of the paper, but suggests that the formation of plg bearing cumulates could happen even more off axis then reported in figure 4. To summarize, the thermo-dynamic calculations confirm that the composition of garnet xenocrysts could be produced by subsolidus metamorphic reactions during the cooling of the lithosphere.

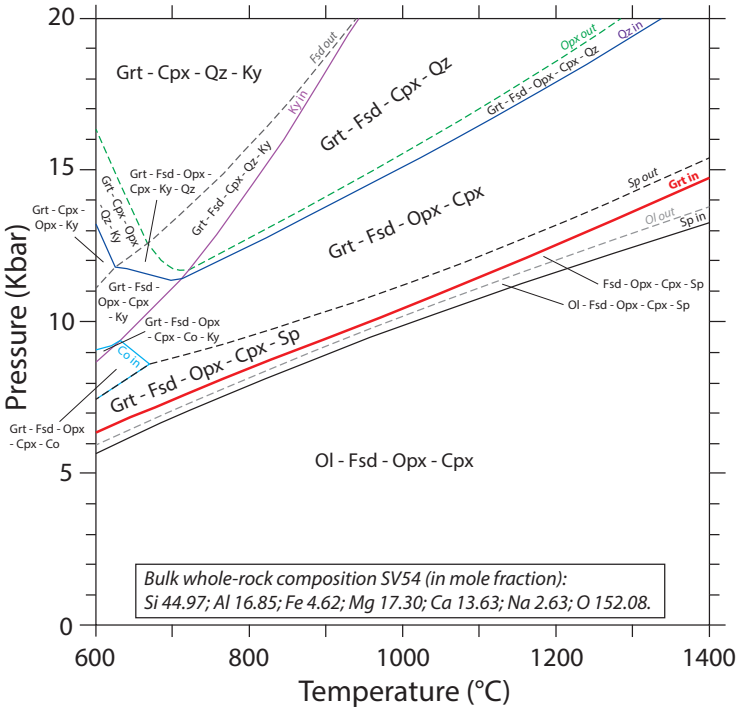

Figure S6: PT diagram calculated with Theriak-Domino. Input composition is experiment SV54 from Villiger et al. (2004) with the following composition in oxide wt%: 49.71 SiO2, 0.30 TiO2, 15.80 Al2O3, 0.11 Cr2O3, 6.10 FeO, 0.13 MnO, 14.06 CaO, 1.50 Na2O, 0.02 K2O. The following abbreviation are used for the reactions listed below: Sp (spinel); Fsp (feldspar plagioclase); Opx (orthopyroxene); Cpx (clinopyroxene); Ol (olivine); Ky (kyanite); Co (corundum); Qz (quartz).

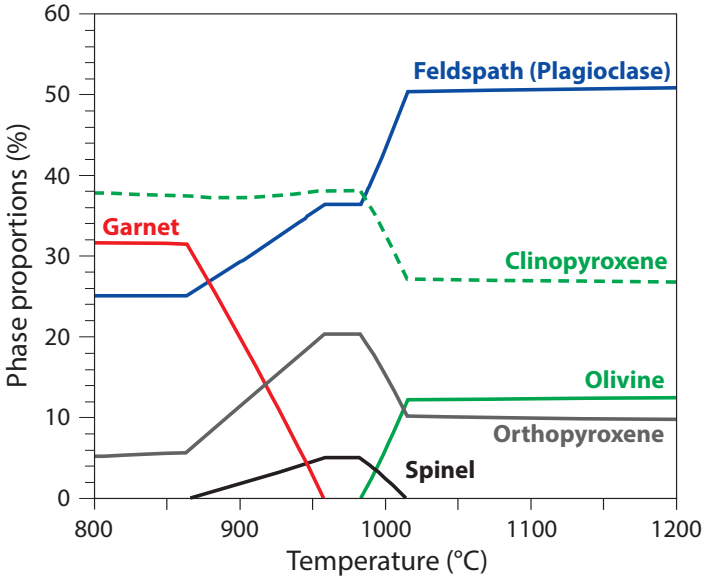

Figure S7. Evolution of phase proportions during the cooling at constant pressure (1 GPa) of a gabbroic cumulate calculated using Theriak-Domino for the composition of Fig. S6 using steps of 1°.

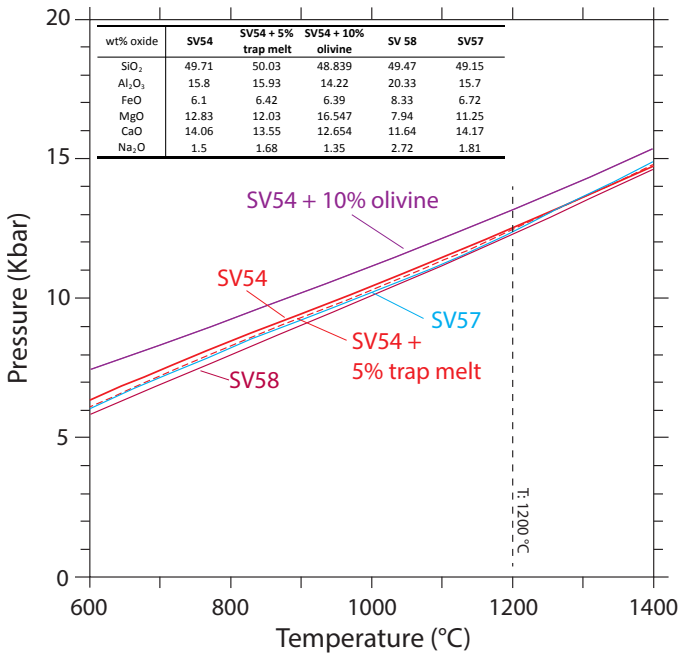

Figure S8. Evaluation of the compositional effect of the starting plg-bearing cumulate on P-T location of plg to garnet subsolidus reaction. The figure reports the position of spinel – feldspath –orthopyroxene – clinopyroxene to garnet – spinel – orthopyroxene –clinopyroxene subsolidus reaction (see Fig. S6) at decreasing temperature for various plg-bearing cumulates predicted by Villiger et al. (2004) experimental study. In addition, we calculate the effect of olivine addition (10%) to plg-bearing cumulate SV 54.

Trace element models as a test for plagioclase-bearing cumulate protolith hypothesis

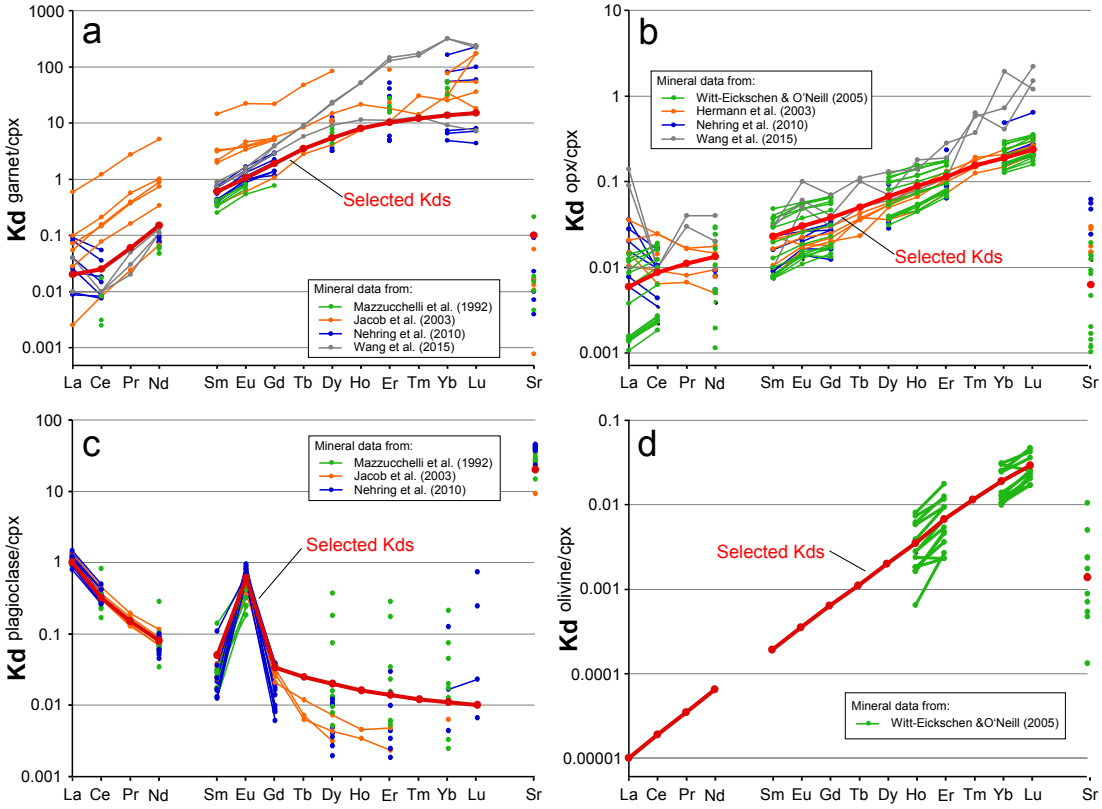

Figure S9: Mineral/cpx partition coefficients ($Kd^{min/cpx}$) for (a) garnet, (b) orthopyroxene, (c) plagioclase, (d) olivine. Red lines and circles show the selected Kd values used in the REE model calculations. Color lines and circles show Kds calculated from mineral analyses reported in various metamorphic and peridotitic rocks (metagabbros: Mazzucchelli *et al.*, 1992a, 1992b; eclogites: Jacob *et al.*, 2003; granulites: Nehring *et al.*, 2010; Wang *et al.*, 2015; gabbro: Hermann et al., 2001; peridotite: Witt-Eickschen & O'Neill, 2005).

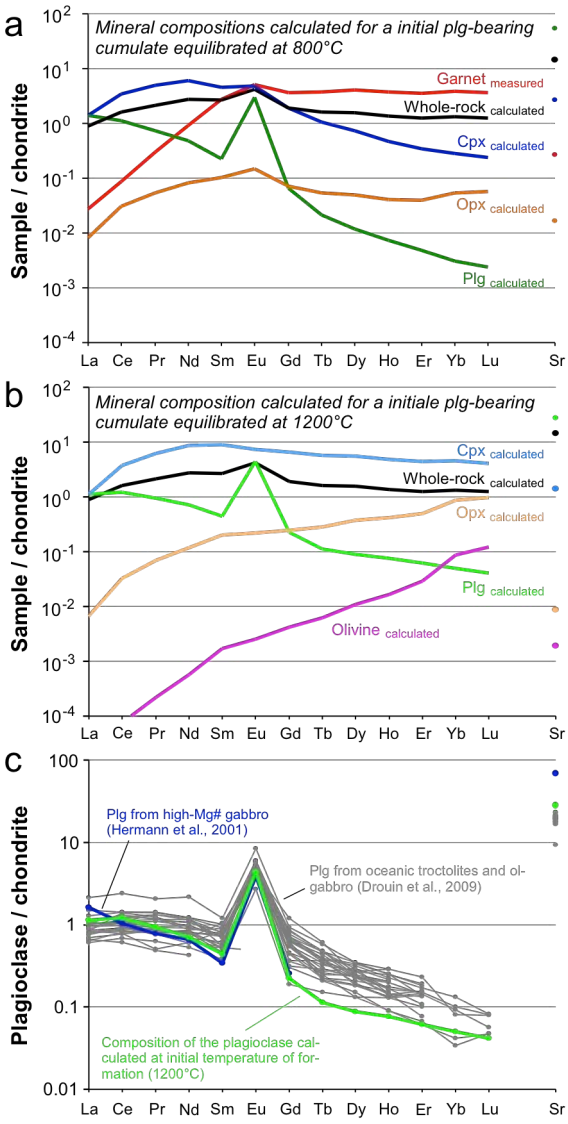

Figure S10 : REE (and Sr) content normalized to chondrite (Anders and Grevesse, 1989) diagrams for a. calculated mineral and whole-rock compositions for a plg-bearing protolith equilibrate at 800°C for a pressure of 1 GPa; b. calculated mineral compositions for a initial plg-bearing protolith equilibrate at 1200°C ; c. calculated plagioclase composition (T: 1200°C) compared with plagioclase from gabbros and (ol-) troctolites (Hermann *et al.*, 2001 ; Drouin *et al.*, 2009). *See text for the details of the calculation*.

We hypothesis that petit-spot garnet xenocryst is formed by isobaric cooling of a plagioclase bearing cumulate at pressure between 0.7 to 1.2 GPa. This metamorphic origin was initially deduced from the similarity between the REE pattern measured in the petit-spot garnet xenocryst and the grt pattern from eclogitic xenoliths from the Roberts Victor kimberlite (Fig. 3b). These eclogites were interpreted by Jacob et al. (2003) as oceanic gabbro subducted to eclogite facies conditions followed by accretion to the Kaapvaal cratonic lithosphere. The figure S7 shows, however, that garnet formed in the 0.7 to 1.2 GPa pressure range still co-exists with plagioclase. This differs from eclogite where the plagioclase was totally consumed to produce garnet and omphacite. In order to potential clarify the protolith composition and evaluate if the positive anomaly observed in garnet xenocrysts (Eu_n/Eu_n^*= 1.7) could be linked to a plagioclase-bearing protolith equilibrated at pressures where plagioclase still co-exist, we develop a REE model.

The model is based on the assumption that garnet is equilibrated with all other phases present in the subsolidus assemblage. This assumption allows to use mineral - mineral distribution coefficients (Kd $^{min/min}$) to infer the composition of the co-existing phase. The figure S9 shows a selection of Kd $^{min/cpx}$ determined in various metamorphic and peridotitic rocks. Based on this compilation, we have selected representative Kd $^{min/cpx}$ for all phases inferred in the subsolidus assemblage (garnet, orthopyroxene, plagioclase, and olivine; Fig. S9). The figure S9 indicates that the absolute values of these Kds could vary for more then one order of magnitude depending the analyzed rocks. Nevertheless, the interrelationship between Kds for different elements does not vary significantly, so the absolute values of calculated mineral and whole rock compositions are expected to vary, but the shape of the patterns will be preserved. The proportion of phases calculated using Theriak-Domino for a gabbroic protolith at 800°C assuming a pressure of 1 GPa (Fig. S7; phase proportion: grt 31.73%, cpx 37.89%, plg 25.15%, opx 5.23%) was used to calculate the whole-rock REE (and Sr) composition of the protolith (Fig. S10a). As shown in figure 3c, this calculated composition is similar to the composition of gabbroic rocks from oceanic lithosphere and support our hypothesis for the origin of petit-spot garnet xenocryst protolith. Nevertheless, the large uncertainty associated to the selection of representative Kds $^{min/cpx}$ does not allow to determine with precision the exact REE content of the protolith, i.e. the interrelationship between elements in the protolith will be conserved, in particular the small positive Eu anomaly, but the REE content could vary significantly according to different choices of Kds.

We have recalculated, in addition, the composition of the phases equilibrated at 1200°C using phase proportion provided by Theriak-Domino (Fig. S7), the protolith whole-rock composition calculated previously and selected Kds. The calculated mineral REE compositions are shown in figure S10b while the figure S10c compares the calculated REE pattern for plagioclase with plagioclase from oceanic rocks. The calculated REE plg pattern is similar to plg patterns of natural rocks (panel c) and no other calculated

phases are characterized by positive Eu anomalies (panel b). These calculations confirm that the positive Eu anomaly observed in garnet xenocryst could be simply linked to the presence of plagioclase in the initial protolith and our interpretation of the formation of the garnet xenocryst as mineral formed during subsolidus reequilibration of plagioclase-bearing protolith is realistic. In addition, the presence of a small positive Eu anomaly in the calculated protolith points to a plagioclase-bearing cumulate origin for the protolith rather than of a gabbro corresponding to freezing basaltic melts within the base of the lithosphere. The uncertainties linked to the Kds (Fig. S9), do not allow, however, to clarify the liquid composition, which produces such cumulates. The similarity of calculated whole-rock cumulate composition with oceanic plagioclase-bearing rocks shown in figure 3 suggests that such a liquid could be similar to MORB, but we can't exclude that this liquid represent slightly lower degree of partial melting of DMM peridotite or tholeiitic melts produced from volatile rich peridotite or pyroxenite. The need of a tholeiitic melt is supported by the request of an early crystallization of plagioclase with cpx and olivine to explain the high Mg# of the garnet xenocryst, plagioclase crystallization which append later in alkaline systems.

Garnet xenocrysts as residual garnet after MORB extraction: implications for REE pattern

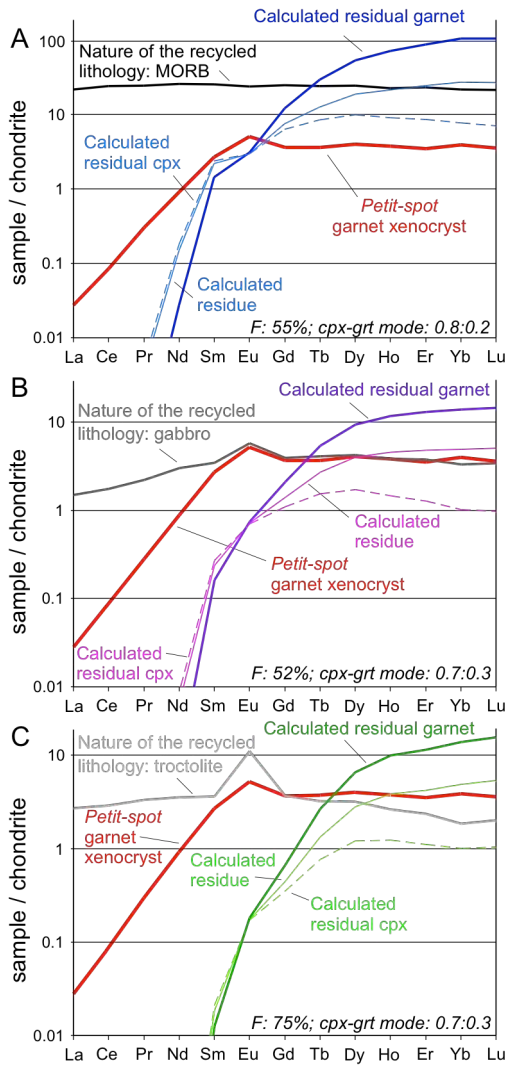

Figure S11 : REE content normalized to chondrite (Anders and Grevesse, 1989) diagrams for calculated residual garnets formed after melt extraction in mid-ocean ridge compared to petit-spot garnet xenocryst. The different panels report garnet compositions calculated assuming a recycled lithology similar in composition to (A) MORB, (B) gabbro, and (C) troctolite. *F*: degree of partial melting in %. *cpx-grt mode* reports the proportion of cpx versus garnet in the starting material. *See text for the list of parameters used in these calculations.*

One hypothesis to explain the presence of garnet within the oceanic lithospheric mantle is that garnet represents garnet from a recycled lithology, which was incorporated into the cooling lithosphere in periphery of mid-ocean ridges. Recycled oceanic crust is frequently suggested to be present in the source of MORB or OIB to explain some aspects of their chemical signatures (e.g. Hirschmann and Stolper, 1996). Pyroxenites/eclogites are characterized by a lower solidus that peridotite, so they are expected to melt first during upwelling of a heterogeneous mantle (Hirschmann and Stolper, 1996). For this reason, the incorporation into the Pacific lithosphere of garnet with composition similar to recycled oceanic crust is unlikely. However, we cannot rule out that residual garnet from recycled crustal lithologies was still present after melt extraction below mid ocean ridges. To evaluate the degree of melting of recycled lithology reaches in such a context, we use the Melt-PX parameterization of Lambart et al. (2016) for pyroxenite melting between 0.9 to 5 GPa. The melting behavior of pyroxenite embedded in peridotite is controlled by the composition of the pyroxenite. As we don't know the composition of the initial recycled lithology, we test different compositions: average MORB (Gale et al., 2013), average gabbro (Mg# 90-76) from PetDb database and a troctolite composition (Kaczmarek et al., 2008).

We assume in our calculation that the source is composed of 10% pyroxenite embedded in 90% of peridotite, a mantle potential temperature of 1350°C, and that the residue escapes the melting process at 1 GPa (~30 km depth). Melt-Px parametrization predicts that a pyroxenite similar to average MORB will reach 55% of melting at 1 GPa. For similar conditions, the degree reaches 52% for average oceanic gabbro, and 75% for a troctolite composition. So, it is possible that garnet could survive the melting process below mid-ocean ridges. But the melting process will modify the trace element content of the residual garnet. We perform fractional melting calculation to evaluate this effect. The Kds $^{grt/liq}$ and Kds $^{cpx/lid}$ reported for tholeiitic magma by Green et al. (2000) was used for fractional melting calculation. Modal melting was used for recycled lithologies according melting experiment mode reported by Pertermann and

Hirschmann (2003) or Kogiso et al. (2006). These experimental results was also used to adjust the amount of cpx versus garnet in the starting material (80:20 for MORB related lithology, while 70:30 was used for gabbro and troctolite). The figure S11 shows that all garnet residues are characterized by high HREE / MREE ratios and extremely low LREE content. Changing the melting mode or mineral mode does not modify significantly the predicted garnet pattern. The absolute REE contents in residual garnet is partially controlled by the initial lithology, but none of the predict garnet pattern reproduces the flat MREE to HREE pattern measured in the petit-spot garnet xenocryst. Assuming batch melting rather that fractional melting increases the LREE to MREE content in the residual garnet but does not modify significantly the HREE to MREE ratio. Based on these calculations, we conclude that it is unlikely that garnet xenocryst sampled by petit-spot lava represent melting residue of recycled lithologies incorporated within the cooling lithosphere after MORB extraction.

Sensitivity to oceanic plate thermal models

The P-T estimates reported for the reaction from plagioclase to garnet via subsolidus cooling allows to estimate the distance from the ridge at which melts need to percolate and freeze to produce the initial plg-bearing cumulate (Fig. 4b). The thermal structure of figure 4b was calculated assuming lithostatic pressure and temperature-dependent density using the plate model (McKenzie 1967), which is formulated as:

$$T(x,z) = T_m\left[-\frac{z}{H} + \sum_{n=1}^{\infty}\frac{2}{n\pi}\exp\left(-\beta\frac{x}{H}\right)\sin\left(-\frac{n\pi z}{H}\right)\right]$$

where H and T_m respectively stand for the plate thickness and adiabatic mantle temperature. The parameter β is calculated as $\beta = \sqrt{R^2 + n^2\pi^2} - R$ where $R = \frac{vH}{2\kappa}$, v (=5 cm/y) stands for the plate velocity estimated for the Pacific plate (Nakanishi *et al.*, 1989; Ritzwoller *et al.*, 2004) and κ (=10^{-6} m^2/s) is the thermal diffusivity. The volumetric mass was calculated according to the following equation of state:

$$\rho(T,P) = \rho_0(1 - \alpha T + \beta P)$$

where ρ_0(=3330 kg/m^3), α (=3.15 K^{-1}), and β (=10^{-11} Pa^{-1}) respectively stand for the reference density, the thermal expansivity, and the compressibility. The pressure field was evaluated using the lithostatic formula:

$$P(z) = -\rho g z$$

where g (=9.81 m/s^2) represents the gravitational acceleration. In figure 4b we have used an adiabatic mantle temperature of 1300˚C and a plate thickness of 100 km. To prove the robustness of our conclusions regarding the locus of formation of plagioclase-bearing cumulate, we have tested alternative oceanic plate thermal models (Fig. S11). While the GDH1 model (Stein & Stein, 1992) and PSM model (Parsons & Sclater, 1977) are based on the above described plate model, the halfspace cooling model is expressed as:

$$T(x,z) = T_m\mathrm{erf}\left(-\frac{z}{2\sqrt{\kappa\frac{x}{v}}}\right).$$

The figure S11 show that, for any of the models, the conditions for the formation of plagioclase-bearing cumulate cannot be met in the vicinity of the spreading axis. All models indeed predict the occurrence of the stability region at distances greater 150 km from the spreading axis (Fig. 4b and Fig. S12). The parameters used for the different models are listed in the following table.

Parameters used in the different models reported in figure 4b and S9.

	Fig. 4	GHD1	PSM	Halfspace cooling
T_m(˚C)	1300	1450	1333	1300
H (km)	100	95	125	-

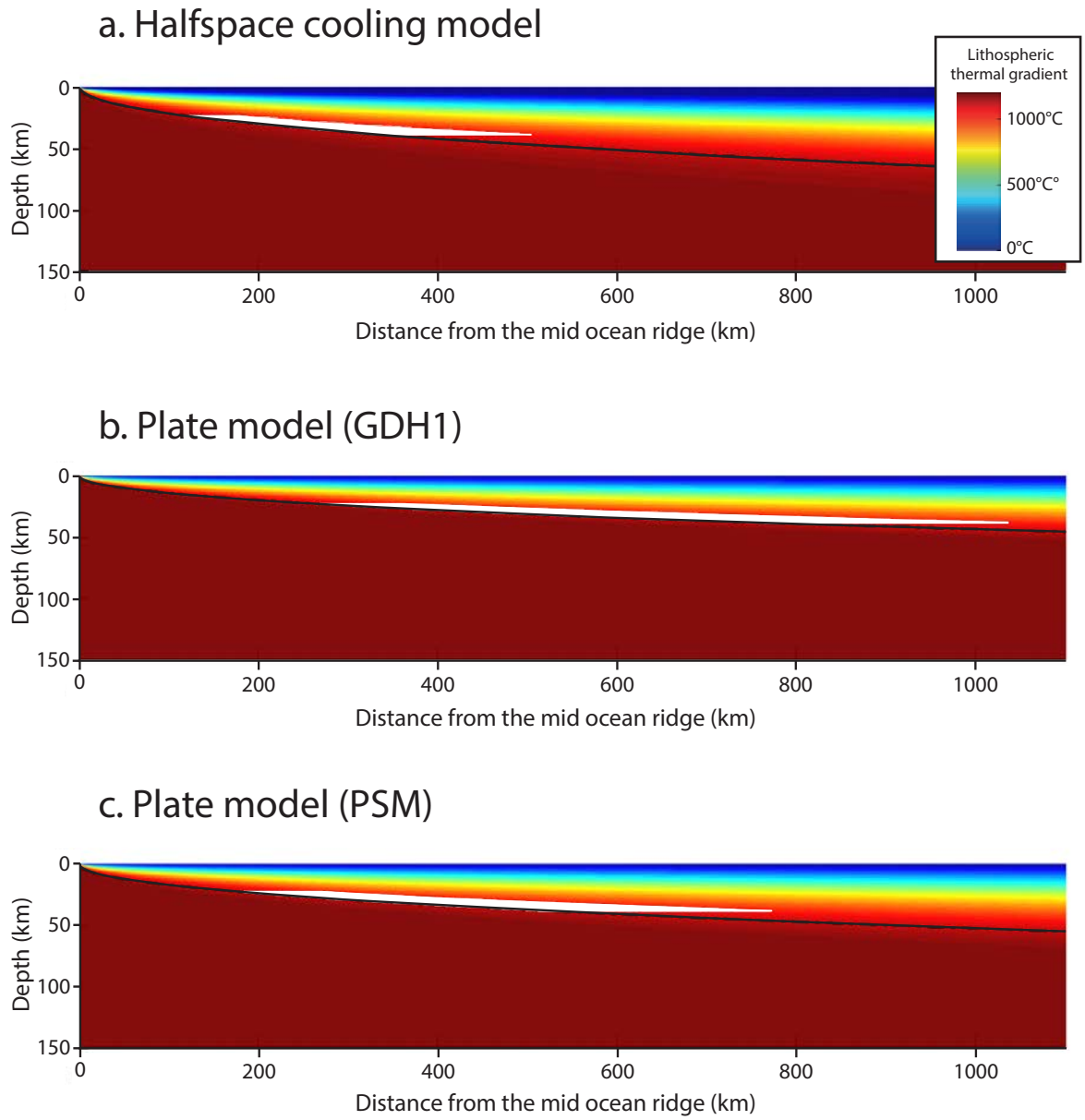

Figure S12. Comparison of thermal structure of an oceanic lithosphere calculated using the halfspace cooling model, GDH1 and PSM plate models (parameters are listed in the overlying table, half-spreading rate of 5 cm yr-1). The white boxes illustrate the P-T conditions, deduced from P-T condition reported in fig 4a, required to produce gabbroic cumulates that will generate garnet by subsolidus cooling. This comparison shows that, even the location of gabbroic cumulates formation varies depending the model, all calculations point out condition for the formation plg-bearing cumulate significantly off ridge axis (>150 km).

References

Aranovich, L. Y., and Berman, R. G., 1996, Optimized standard state and solution properties of minerals .2. Comparisons, predictions, and applications: Contributions to Mineralogy and Petrology, v. 126, no. 1-2, p. 25-37.

Armstrong, J. T., 1988, Quantitative analysis of silicate and oxide minerals, comparison of Monte Carlo, ZAF and Φ(ρz) procedures, *in* Newbury, D. E., ed., Microbeam Analysis: San Francisco, CA, San Francisco Press, p. 239-246.

Berman, R. G., 1988, Internally-consistent thermodynamic data for minerals in the system Na2O-K2O-CaO-MgO-FeO-Fe2O3-Al2O3-SiO2-TiO2-H2O-CO2: Journal of Petrology, v. 29, no. 2, p. 445-522.

Berman, R. G., 1990, Mixing properties of Ca-Mg-Fe-Mn garnets: American Mineralogist, v. 75, no. 3-4, p. 328-344.

Berman, R. G., and Aranovich, L. Y., 1996, Optimized standard state and solution properties of minerals .1. Model calibration for olivine, orthpyroxene, cordierite, garnet, ilmenite in the system FEO-MGO-CaO-Al2O3-TiO3-SiO2: Contributions to Mineralogy and Petrology, v. 126, no. 1-2, p. 1-24.

Beyer, E. E., Griffin, W. L., and O'Reilly, S. Y., 2006, Transformation of Archaean Lithospheric Mantle by Refertilization: Evidence from Exposed Peridotites in the Western Gneiss Region, Norway: Journal of Petrology, v. 47, no. 8, p. 1611-1636.

Bizimis, M., Sen, G., Salters, V. J. M., and Keshav, S., 2005, Hf-Nd-Sr isotope systematics of garnet pyroxenites from Salt Lake Crater, Oahu, Hawaii: Evidence for a depleted component in Hawaiian volcanism: Geochimica et Cosmochimica Acta, v. 69, no. 10, p. 2629-2646.

Bucher, K., 2005. Blueschists, eclogites, and decompression assemblages of the Zermatt-Saas ophiolite: High-pressure metamorphism of subducted Tethys lithosphere. American Mineralogist, v. 90, no. 5-6, p. 821–835.

Canil, D., and O'Neill, H. S., 1996, Distribution of ferric iron in some upper-mantle assemblages: Journal of Petrology, v. 37, no. 3, p. 609-635.

Clarke, G.L., Aitchison, J.C., Cluzel, D., 1997. Eclogites and blueschists of the Pam Peninsula, NE New Caledonia: a reappraisal: Journal of Petrology, v. 38, no. 7, p. 843–876.

de Capitani, C., and Petrakakis, K., 2010, The computation of equilibrium assemblage diagrams with Theriak/Domino software: American Mineralogist, v. 95, no. 7, p. 1006-1016.

Evans, B. W., Trommsdorff, V., and Richter, W., 1979, Petrology of an eclogite-metarodingite suite at Cima di Gagnone, Ticino, Switzerland: American Mineralogist, v. 64, no 1-2, p. 15-31.

Drouin, M., Godard, M., Ildefonse, B., Brugier, O., and Garrido C.J., 2009, Geochemical and petrographic evidence for magmatic impregnation in the oceanic lithosphere at Atlantis Massif, Mid-Atlantic Ridge (IODP Hole U1309D, 30°N): Chemical Geology, v. 264, p. 71-88.

Green, T. H., Blundy, J. D., Adam, J., and Yaxley, G. M., 2000, SIMS determination of trace element partition coefficients between garnet, clinopyroxene and hydrous basaltic liquids at 2-7.5 GPa and 1080-1200 degrees C: Lithos, v. 53, no. 3-4, p. 165-187.

Gregoire, M., Bell, D. R., and Le Roex, A. P., 2003, Garnet lherzolites from the Kaapvaal craton (South Africa): Trace element evidence for a metasomatic history: Journal of Petrology, v. 44, no. 4, p. 629-657.

Hermann, J., Müntener, O., and Günther, D., 2001, Differentiation of mafic magma in a continental crust-to-mantle transition zone : Journal of Petrology, v. 42, no. 1, p. 189-206.

Hirano, N., Takahashi, E., Yamamoto, J., Abe, N., Ingle, S.P., 2006. Volcanism in response to plate flexure: Science, v. 313, no. 5792, p. 1426-1428.

Hirschmann, M. M., and Stolper, E. M., 1996, A possible role for garnet pyroxenite in the origin of the “garnet signature” in MORB: Contributions to Mineralogy and Petrology, v. 124, no. 2, p. 185-208.

Ionov, D. A., Ashchepkov, I. V., Stosch, H.-G., Witt-Eickschen, G., and Seck, H. A., 1993, Garnet peridotite xenoliths from the Vitim Volcanic Field, Baikal Region: the nature of the garnet—spinel peridotite transition zone in the continental mantle: Journal of Petrology, v. 34, no. 6, p. 1141-1175.

Ionov, D. A., Doucet, L. S., and Ashchepkov, I. V., 2010, Composition of the Lithospheric Mantle in the Siberian Craton: New Constraints from Fresh Peridotites in the Udachnaya-East Kimberlite: Journal of Petrology, v. 51, no. 11, p. 2177-2210.

Ishikawa, A., Maruyama, S., and Komiya, T., 2004, Layered lithospheric mantle beneath the Ontong Java Plateau: Implications from xenoliths in Alnoite, Malaita, Solomon Islands: Journal of Petrology, v. 45, no. 10, p. 2011-2044.

Jacob, D., Schmickler, B., Schulze, D.J., 2003. Trace element geochemistry of coesite-bearing eclogites from the Roberts Victor kimberlite, Kaapvaal craton: Lithos, v. 71, no. 2-4, p. 337–351.

Jacob, D.E., Foley, S.F., 1999. Evidence for Archean ocean crust with low high field strength element signature from diamondiferous eclogite xenoliths: Lithos, v. 48, no. 1, p. 317–336.

Kaczmarek, M.-A., Müntener, O., and Rubatto, D., 2008, Trace element chemistry and U-Pb dating of zircons from oceanic gabbros and their relationship with whole rock composition: Contributions to Mineralogy and Petrology, v. 155, p. 295-312.

Keshav, S., Sen, G., and Presnall, D. C., 2007, Garnet-bearing Xenoliths from Salt Lake Crater, Oahu, Hawaii: High-Pressure Fractional Crystallization in the Oceanic Mantle: Journal of Petrology, v. 48, no. 9, p. 1681-1724.

King, R.L., Bebout, G.E., Kobayashi, K., Nakamura, E., van der Klauw, S.N.G.C., 2004. Ultrahigh-pressure metabasaltic garnets as probes into deep subduction zone chemical cycling: Geochemistry Geophysics Geosystems, v. 5, no. 12, doi:10.1029/2004GC000746.

Kogiso, T., and Hirschmann M.M., 2006, Partial melting experiments of bimineralic eclogite and the role of recycled mafic oceanic crust in the genesis of ocean island basalts: Earth and Planetary Science Letters, v. 249, no. 3-4, p. 188-199, doi:10.1016/j.epsl.2006.07.016.

Lambart, S., Baker, M.B., and Stolper, E.M. 2016, The role of pyroxenite in basalt genesis: Melt-PX, a melting parameterization for mantle pyroxenites between 0.9 and 5 GPa: Journal of Geophysical Research: Solid Earth, v. 121, doi:10.1002/2015JB012762.

Litasov, K. D., Foley, S. F., and Litasov, Y. D., 2000, Magmatic modification and metasomatism of the subcontinental mantle beneath the Vitim volcanic field (East Siberia): evidence from trace element data on pyroxenite and peridotite xenoliths from Miocene picrobasalt: Lithos, v. 54, no. 1-2, p. 83-114.

Longerich, H. P., Jackson, S. E., and Gunther, D., 1996, Laser ablation inductively coupled plasma mass spectrometric transient signal data acquisition and analyte concentration calculation: Journal of Analytical Atomic Spectrometry, v. 11, no. 9, p. 899-904.

Mazzucchelli M, Rivalenti G., Vannucci R., Bottazzi P., Ottolini L., Hofmann A.W., and Parenti, M., 1992a, Primary positive Eu anomaly in clinopyroxenes of low-crust gabbroic rocks: Geochimica et Cosmochimica Acta, v. 56, no. 6, p. 2363-2370.

Mazzucchelli M, Rivalenti G., Vannucci R., Bottazzi P., Ottolini L., Hofmann A.W., Sinigoi S. and Demarchi G., 1992b, Trace-element distribution between clinopyroxene and garnet in gabbroic rocks of the deep crust: An ion microprobe study: Geochimica et Cosmochimica Acta, v. 56, no. 6, p. 2371-2385.

McKenzie, D., 1967, Some remarks on heat flow and gravity anomalies : Journal of Geophysical Research, v. 72, no. 24, p. 6261–6273.

Meyre, C., DeCapitani, C., and Partzsch, J. H., 1997, A ternary solid solution model for omphacite and its application to geothermobarometry of eclogites from the Middle Adula nappe (Central Alps, Switzerland): Journal of Metamorphic Geology, v. 15, no. 6, p. 687-700.

Nakanishi, M., Tamaki, K., and Kobayashi, K., 1989, Mesozoic magnetic anomaly lineations and seafloor spreading history of the northwestern Pacific: Journal of Geophysical Research-Solid Earth and Planets, v. 94, no. B11, p. 15437-15462.

Nehring, F., Foley, S.F., and Holtta, P., 2010, Trace element partitioning in the granulite facies : Contributions to Mineralogy and Petrology, v. 159, no. 4, p. 493-519.

Parsons, B., and Sclater, J. G., 1977, An analysis of the variation of ocean floor bathymetry and heat flow with age : Journal of Geophysical Research, v. 82, no. 5, p. 803–827.

Peltonen, P., Kinnunen, K. A., and Huhma, H., 2002, Petrology of two diamondiferous eclogite xenoliths from the Lahtojoki kimberlite pipe, eastern Finland: Lithos, v. 63, no. 3–4, p. 151-164.

Pertermann, M., and Hirschmann, M.M., 2003, Partial melting experiments on a MORB-like pyroxenite between 2 and 3 GPa: Constraints on the presence of pyroxenite in basalt source regions from solidus location and melting rate : Journal of Geophysical Research, v. 108, no. B2, 2125, doi:10.1029/2000JB000118.

Pernet-Fisher, J.F., Howarth, G.H., Liu, Y., Barry, P.H., Carmody, L., Valley, J.W., Bodnar, R.J., Spetsius, Z.V., and Taylor, L.A., 2014. Komsomolskaya diamondiferous eclogites: evidence for oceanic crustal protoliths: Contributions to Mineralogy and Petrology, v. 167, no. 3, p. 981, doi:10.1007/s00410-014-0981-y

Ritzwoller, M. H., Shapiro, N. M., and Zhong, S.-J., 2004, Cooling history of the Pacific lithosphere: Earth and Planetary Science Letters, v. 226, no. 1-2, p. 69-84.

Scambelluri, M., Pettke, T., Rampone, E., GODARD, M., and Reusser, E., 2014, Petrology and Trace Element Budgets of High-pressure Peridotites Indicate Subduction Dehydration of Serpentinized Mantle (Cima di Gagnone, Central Alps, Switzerland): Journal of Petrology, v. 55, no. 3, p. 459-498.

Schulze, D.J., Valley, J.W., Spicuzza, M.J., 2000. Coesite eclogites from the Roberts Victor kimberlite, South Africa: Lithos, v. 54, no. 1, p. 23–32.

Simon, N., 2003, The origin of garnet and clinopyroxene in “depleted” Kaapvaal peridotites: Lithos, v. 71, no. 2-4, p. 289-322.

Smart, K. A., Heaman, L. M., Chacko, T., Simonetti, A., Kopylova, M., Mah, D., and Daniels, D., 2009, The origin of high-MgO diamond eclogites from the Jericho Kimberlite, Canada: Earth and Planetary Science Letters, v. 284, no. 3-4, p. 527-537.

Stein, C. A., and Stein, S., 1992, A model for the global variation in oceanic depth and heat flow with lithospheric age: Nature, v. 359, p. 123-129.

Tappe, S., Smart, K. A., Pearson, D. G., Steenfelt, A., and Simonetti, A., 2011, Craton formation in Late Archean subduction zones revealed by first Greenland eclogites: Geology, v. 39, no. 12, p. 1103-1106.

van Achterbergh, E., Griffin, W. L., and Stiefenhofer, J., 2001, Metasomatism in mantle xenoliths from the Letlhakane kimberlites: estimation of element fluxes: Contributions to Mineralogy and Petrology, v. 141, no. 4, p. 397-414.

Villiger, S., Ulmer, P., Muntener, O., and Thompson, A. B., 2004, The liquid line of descent of anhydrous, mantle-derived, tholeiitic liquids by fractional and equilibrium crystallization - an experimental study at 1 center dot 0 GPa: Journal of Petrology, v. 45, no. 12, p. 2369-2388.

Wang, H.Z., Zhang, H.F., and Zhai, M.G., 2015, Trace element redistributed patterns in rock-forming minerals of mafic granulite as indicators for metamorphic history: A case study of high-pressure granulite from the Jiaobei terrane, North China Craton. Acta Petrologica Sinica, v. 31, no. 6, p. 1694-1710.

Witt-Eickschen, G. and O'Neill, H.S.C., 2005, The effect of temperature on the equilibrium distribution of trace elements between clinopyroxene, orthopyroxene, olivine and spinel in upper mantle peridotite : Chemical Geology, v. 221, no. 1-2, p. 65-101.

Ziberna, L., Nimis, P., Zanetti, A., Marzoli, A., and Sobolev, N. V., 2013, Metasomatic Processes in the Central Siberian Cratonic Mantle: Evidence from Garnet Xenocrysts from the Zagadochnaya Kimberlite: Journal of Petrology, v. 54, no. 11, p. 2379-2409.

Table S1: Representative analyses of petit-spot garnet xenocryst (Profile 4; Fig. S1a)

	Kelyphite rim															
	L 002	L 004	L 013	L 014	L 016	L 018	L 019	L 020	L 021	L 022	L 023	L 024	L 025	L 026	L 027	L 028
SiO_2	42.05	39.74	41.78	40.98	41.33	41.50	41.83	41.93	42.22	41.33	40.87	40.96	41.14	40.98	42.56	42.16
TiO_2	0.19	0.13	0.13	0.12	0.13	0.15	0.13	0.12	0.14	0.09	0.13	0.10	0.12	0.10	0.14	0.15
Cr_2O_3	0.08	0.17	0.11	0.13	0.13	0.14	0.13	0.10	0.12	0.14	0.13	0.15	0.18	0.14	0.14	0.18
Al_2O_3	20.83	22.13	23.55	24.32	24.05	23.75	23.81	23.07	23.69	22.86	23.28	23.82	22.32	23.04	23.05	23.34
FeO	9.28	8.97	7.14	7.81	7.13	7.59	6.95	7.89	7.56	8.88	9.20	8.11	8.86	8.92	8.93	9.41
MnO	0.16	0.16	0.13	0.16	0.16	0.13	0.12	0.16	0.15	0.18	0.17	0.15	0.18	0.17	0.17	0.19
NiO	0.00	0.00	0.00	0.00	0.00	0.00	0.00	0.00	0.00	0.00	0.00	0.00	0.00	0.00	0.00	0.00
MgO	19.20	19.20	15.35	16.23	15.63	15.73	15.19	16.73	15.65	17.98	18.24	16.70	19.08	17.65	18.14	18.55
CaO	8.24	7.63	8.53	7.22	7.67	7.52	8.09	7.56	7.49	6.74	6.07	7.54	6.10	6.45	6.84	6.95
Na_2O	1.13	1.13	1.67	1.54	1.71	1.50	1.42	1.40	1.69	1.26	1.34	1.20	1.08	1.08	0.61	0.19
K_2O	0.23	0.28	1.35	1.36	1.64	1.58	1.48	1.51	1.63	1.23	1.53	1.34	1.43	1.54	0.71	0.07
Total	101.39	99.53	99.74	99.87	99.57	99.58	99.15	100.48	100.33	100.69	100.97	100.07	100.50	100.07	101.29	101.19

	Garnet core																				
	L 029	L 030	L 031	L 033	L 034	L 035	L 036	L 037	L 038	L 042	L 046	L 049	L 050	L 051	L 052	L 053	L 054	L 056	L 057	L 058	L 059
SiO_2	42.38	42.32	41.93	41.83	41.83	41.84	42.36	42.13	42.00	42.14	42.17	42.50	42.34	42.86	42.66	41.76	42.35	42.75	42.57	41.56	42.34
TiO_2	0.11	0.13	0.10	0.13	0.10	0.13	0.16	0.14	0.14	0.12	0.15	0.12	0.12	0.17	0.15	0.12	0.11	0.13	0.12	0.13	0.10
Cr_2O_3	0.12	0.11	0.12	0.17	0.14	0.14	0.17	0.15	0.18	0.15	0.12	0.17	0.13	0.15	0.14	0.16	0.10	0.16	0.10	0.09	0.13
Al_2O_3	23.46	24.06	23.26	22.98	23.84	22.19	22.23	22.77	22.95	23.35	22.84	22.71	23.38	23.21	23.17	23.24	23.59	24.26	23.89	22.19	24.08
FeO	8.71	8.30	9.15	9.88	8.33	9.65	9.86	8.93	9.18	8.68	9.07	9.73	8.85	9.46	9.06	8.80	8.45	8.21	8.50	9.20	8.28
MnO	0.19	0.16	0.18	0.20	0.14	0.24	0.18	0.20	0.19	0.18	0.17	0.19	0.16	0.19	0.19	0.17	0.17	0.16	0.18	0.20	0.16
NiO	0.00	0.00	0.00	0.00	0.00	0.00	0.00	0.00	0.00	0.00	0.00	0.00	0.00	0.00	0.00	0.00	0.00	0.00	0.00	0.00	0.00
MgO	17.14	15.92	17.41	18.81	15.86	18.33	18.33	17.02	17.14	16.70	17.40	18.33	17.07	17.95	17.98	17.03	16.39	16.51	16.85	17.72	16.64
CaO	7.92	8.94	8.28	6.87	9.00	7.39	7.38	8.10	7.91	7.99	7.56	6.53	8.31	7.20	7.35	8.42	8.84	8.24	8.85	8.58	8.38
Na_2O	0.17	0.06	0.03	0.00	0.03	0.06	0.03	0.03	0.06	0.08	0.06	0.05	0.04	0.03	0.05	0.05	0.01	0.04	0.05	0.04	0.02
K_2O	0.02	0.00	0.00	0.01	0.01	0.00	0.01	0.00	0.01	0.00	0.01	0.01	0.00	0.00	0.00	0.00	0.00	0.01	0.01	0.01	0.00
Total	100.22	100.01	100.46	100.88	99.28	99.97	100.70	99.48	99.76	99.38	99.55	100.35	100.40	101.23	100.75	99.75	100.02	100.47	101.12	99.72	100.14
Numbers of ions on 12 Oxygen																					
Si	3.026	3.040	2.990	2.962	3.027	2.993	3.012	3.038	3.019	3.040	3.034	3.029	3.023	3.033	3.028	3.000	3.040	3.051	3.017	2.983	3.030
Ti	0.006	0.007	0.005	0.007	0.005	0.007	0.008	0.008	0.008	0.006	0.008	0.007	0.007	0.009	0.008	0.006	0.006	0.007	0.006	0.007	0.005
Cr	0.007	0.006	0.007	0.009	0.008	0.008	0.009	0.009	0.010	0.008	0.007	0.009	0.007	0.008	0.008	0.009	0.005	0.009	0.005	0.005	0.008
Al4	0.000	0.000	0.010	0.038	0.000	0.007	0.000	0.000	0.000	0.000	0.000	0.000	0.000	0.000	0.000	0.000	0.000	0.000	0.000	0.017	0.000
Al6	1.975	2.037	1.944	1.879	2.034	1.864	1.863	1.935	1.945	1.986	1.937	1.908	1.968	1.936	1.939	1.967	1.996	2.041	1.996	1.861	2.031
Fe3+	0.000	0.000	0.053	0.136	0.000	0.129	0.091	0.000	0.001	0.000	0.000	0.019	0.000	0.000	0.000	0.018	0.000	0.000	0.000	0.144	0.000
Fe2+	0.520	0.499	0.492	0.449	0.504	0.449	0.495	0.538	0.551	0.524	0.546	0.561	0.528	0.560	0.538	0.510	0.507	0.490	0.504	0.409	0.496
Mn	0.012	0.010	0.011	0.012	0.008	0.015	0.011	0.012	0.012	0.011	0.010	0.012	0.010	0.012	0.011	0.010	0.011	0.010	0.011	0.012	0.010
Ni	0.000	0.000	0.000	0.000	0.000	0.000	0.000	0.000	0.000	0.000	0.000	0.000	0.000	0.000	0.000	0.000	0.000	0.000	0.000	0.000	0.000
Mg	1.824	1.704	1.850	1.985	1.711	1.954	1.943	1.829	1.836	1.796	1.866	1.947	1.817	1.893	1.902	1.823	1.753	1.756	1.780	1.896	1.775
Ca	0.606	0.688	0.632	0.521	0.698	0.566	0.562	0.626	0.609	0.618	0.583	0.499	0.636	0.546	0.559	0.648	0.680	0.630	0.672	0.660	0.643
Na	0.023	0.009	0.005	0.000	0.004	0.008	0.004	0.004	0.009	0.011	0.009	0.007	0.005	0.004	0.007	0.007	0.002	0.005	0.007	0.006	0.002
K	0.002	0.000	0.000	0.001	0.001	0.000	0.001	0.000	0.001	0.000	0.001	0.001	0.000	0.000	0.000	0.000	0.000	0.001	0.001	0.001	0.000
Total	8.000	8.000	8.000	8.000	8.000	8.000	8.000	8.000	8.000	8.000	8.000	8.000	8.000	8.000	8.000	8.000	8.000	8.000	8.000	8.000	8.000

	Garnet core																				
	L 060	L 061	L 062	L 063	L 064	L 065	L 066	L 070	L 071	L 072	L 073	L 074	L 075	L 076	L 078	L 080	L 082	L 083	L 084	L 085	L 086
SiO_2	42.54	42.37	42.49	42.32	42.18	42.22	42.76	42.30	42.86	42.34	42.61	42.76	41.76	42.27	41.64	41.85	41.94	41.96	41.70	41.87	42.89
TiO_2	0.10	0.10	0.11	0.15	0.16	0.11	0.14	0.14	0.15	0.12	0.11	0.14	0.14	0.09	0.11	0.15	0.13	0.11	0.12	0.14	0.13
Cr_2O_3	0.16	0.16	0.11	0.14	0.17	0.12	0.13	0.15	0.12	0.15	0.14	0.14	0.13	0.11	0.13	0.11	0.13	0.13	0.13	0.16	0.14
Al_2O_3	23.03	23.68	23.67	23.41	23.66	23.31	23.66	23.34	23.58	23.49	23.78	23.55	23.23	22.75	23.79	22.71	23.89	24.17	23.13	23.35	23.33
FeO	8.84	9.00	8.53	9.47	8.99	9.13	8.86	8.74	8.79	8.90	8.66	8.83	9.18	9.01	8.64	9.57	8.36	9.05	9.34	9.22	8.84
MnO	0.21	0.17	0.18	0.17	0.18	0.19	0.19	0.21	0.19	0.19	0.19	0.19	0.20	0.19	0.17	0.17	0.16	0.18	0.20	0.19	0.19
NiO	0.00	0.00	0.00	0.00	0.00	0.00	0.00	0.00	0.00	0.00	0.00	0.00	0.00	0.00	0.00	0.00	0.00	0.00	0.00	0.00	0.00
MgO	17.32	17.72	16.38	18.01	17.25	17.28	17.21	17.46	17.21	17.39	17.11	17.42	17.43	17.59	17.16	18.54	16.15	16.94	17.77	17.98	17.48
CaO	8.19	8.11	8.53	7.45	7.96	8.18	7.95	7.36	8.15	8.33	8.01	7.94	7.49	8.49	8.33	7.64	9.55	8.47	8.09	7.99	7.88
Na_2O	0.04	0.04	0.03	0.03	0.03	0.03	0.04	0.05	0.02	0.03	0.01	0.05	0.02	0.01	0.03	0.01	0.06	0.02	0.02	0.03	0.03
K_2O	0.00	0.00	0.01	0.01	0.00	0.00	0.00	0.00	0.00	0.00	0.00	0.00	0.01	0.00	0.00	0.00	0.00	0.00	0.00	0.00	0.00
Total	100.43	101.34	100.05	101.17	100.57	100.58	100.94	99.76	101.07	100.94	100.63	101.02	99.59	100.51	100.00	100.74	100.37	101.03	100.49	100.93	100.92
Numbers of ions on 12 Oxygen																					
Si	3.035	2.991	3.049	2.993	3.005	3.009	3.036	3.034	3.040	3.005	3.034	3.031	3.003	3.012	2.980	2.968	3.000	2.978	2.970	2.967	3.044
Ti	0.005	0.005	0.006	0.008	0.009	0.006	0.008	0.008	0.008	0.006	0.006	0.007	0.008	0.005	0.006	0.008	0.007	0.006	0.006	0.008	0.007
Cr	0.009	0.009	0.006	0.008	0.010	0.007	0.007	0.009	0.007	0.008	0.008	0.008	0.008	0.006	0.007	0.006	0.007	0.007	0.007	0.009	0.008
Al4	0.000	0.009	0.000	0.007	0.000	0.000	0.000	0.000	0.000	0.000	0.000	0.000	0.000	0.000	0.020	0.032	0.000	0.022	0.030	0.033	0.000
Al6	1.937	1.962	2.002	1.945	1.987	1.958	1.980	1.973	1.971	1.965	1.996	1.968	1.969	1.911	1.986	1.867	2.014	2.000	1.912	1.917	1.952
Fe3+	0.000	0.033	0.000	0.043	0.000	0.009	0.000	0.000	0.000	0.008	0.000	0.000	0.006	0.050	0.019	0.146	0.000	0.006	0.101	0.097	0.000
Fe2+	0.527	0.498	0.512	0.517	0.536	0.535	0.526	0.524	0.521	0.520	0.516	0.523	0.546	0.487	0.498	0.422	0.500	0.532	0.456	0.450	0.525
Mn	0.013	0.010	0.011	0.010	0.011	0.012	0.011	0.013	0.012	0.011	0.011	0.012	0.012	0.012	0.010	0.010	0.010	0.011	0.012	0.011	0.012
Ni	0.000	0.000	0.000	0.000	0.000	0.000	0.000	0.000	0.000	0.000	0.000	0.000	0.000	0.000	0.000	0.000	0.000	0.000	0.000	0.000	0.000
Mg	1.842	1.864	1.752	1.899	1.832	1.836	1.821	1.867	1.819	1.839	1.816	1.841	1.868	1.868	1.830	1.960	1.722	1.792	1.886	1.899	1.849
Ca	0.626	0.613	0.656	0.565	0.608	0.625	0.605	0.566	0.619	0.633	0.611	0.603	0.577	0.648	0.639	0.580	0.732	0.644	0.617	0.607	0.599
Na	0.006	0.005	0.005	0.004	0.003	0.004	0.005	0.007	0.002	0.004	0.002	0.007	0.003	0.001	0.004	0.002	0.009	0.003	0.002	0.004	0.004
K	0.000	0.000	0.001	0.001	0.000	0.000	0.000	0.000	0.000	0.000	0.000	0.000	0.001	0.000	0.000	0.000	0.000	0.000	0.000	0.000	0.000
Total	8.000	8.000	8.000	8.000	8.000	8.000	8.000	8.000	8.000	8.000	8.000	8.000	8.000	8.000	8.000	8.000	8.000	8.000	8.000	8.000	8.000

Table S1 (suite): Representative analyses of petit-spot garnet xenocryst (Profile 4; Fig. S1a)

	Garnet core (suite)																				
	L 087	L 088	L 089	L 090	L 092	L 093	L 094	L 096	L 097	L 098	L 102	L 103	L 104	L 108	L 109	L 110	L 111	L 112	L 114	L 115	L 116
SiO_2	42.15	42.42	42.16	42.22	41.89	42.23	42.61	42.25	42.47	42.01	42.54	42.35	42.59	42.24	42.62	42.09	42.18	42.67	42.14	42.09	42.36
TiO_2	0.13	0.15	0.14	0.14	0.11	0.11	0.12	0.11	0.13	0.14	0.14	0.13	0.14	0.12	0.11	0.15	0.11	0.12	0.10	0.15	0.14
Cr_2O_3	0.14	0.18	0.14	0.15	0.11	0.15	0.10	0.11	0.13	0.18	0.14	0.14	0.16	0.14	0.08	0.14	0.11	0.15	0.15	0.10	0.17
Al_2O_3	23.51	24.02	23.72	23.65	23.64	24.16	22.99	23.15	23.67	22.72	24.06	23.40	23.73	23.20	24.52	23.38	22.85	23.19	23.54	23.42	23.98
FeO	9.64	8.80	8.52	8.70	9.18	8.08	8.76	9.43	8.77	9.74	8.52	9.49	9.24	8.86	7.67	9.45	9.46	9.27	9.08	8.74	9.06
MnO	0.20	0.17	0.17	0.18	0.20	0.18	0.20	0.21	0.19	0.19	0.20	0.18	0.20	0.20	0.16	0.19	0.19	0.18	0.19	0.19	0.19
NiO	0.00	0.00	0.00	0.00	0.00	0.00	0.00	0.00	0.00	0.00	0.00	0.00	0.00	0.00	0.00	0.00	0.00	0.00	0.00	0.00	0.00
MgO	18.17	17.00	16.76	16.61	17.41	15.83	17.57	18.18	17.17	19.06	16.61	18.26	17.54	17.53	15.00	18.00	18.12	17.82	17.33	17.19	17.30
CaO	7.41	7.91	8.62	8.68	8.02	9.24	8.00	7.62	8.09	6.84	8.25	7.43	7.54	8.42	9.41	7.63	7.83	8.02	7.86	8.36	7.87
Na_2O	0.04	0.01	0.04	0.04	0.01	0.03	0.03	0.04	0.01	0.02	0.02	0.04	0.04	0.03	0.03	0.05	0.04	0.03	0.04	0.04	0.02
K_2O	0.01	0.00	0.00	0.00	0.00	0.01	0.00	0.00	0.01	0.01	0.00	0.00	0.00	0.00	0.01	0.00	0.00	0.00	0.01	0.00	0.00
Total	101.40	100.65	100.28	100.37	100.57	100.01	100.38	101.10	100.65	100.91	100.47	101.42	101.18	100.75	99.61	101.08	100.88	101.45	100.44	100.27	101.09
Numbers of ions on 12 Oxygen																					
Si	2.973	3.021	3.014	3.019	2.983	3.033	3.039	2.988	3.024	2.971	3.038	2.986	3.015	3.002	3.079	2.979	2.991	3.012	3.005	3.006	3.003
Ti	0.007	0.008	0.008	0.008	0.006	0.006	0.006	0.006	0.007	0.008	0.007	0.007	0.007	0.007	0.006	0.008	0.006	0.006	0.005	0.008	0.008
Cr	0.008	0.010	0.008	0.008	0.006	0.008	0.006	0.006	0.007	0.010	0.008	0.008	0.009	0.008	0.004	0.008	0.006	0.009	0.008	0.005	0.009
Al4	0.027	0.000	0.000	0.000	0.017	0.000	0.000	0.012	0.000	0.029	0.000	0.014	0.000	0.000	0.000	0.021	0.009	0.000	0.000	0.000	0.000
Al6	1.928	2.017	1.999	1.993	1.968	2.046	1.932	1.918	1.986	1.865	2.025	1.930	1.980	1.943	2.088	1.929	1.901	1.930	1.979	1.972	2.004
Fe3+	0.084	0.000	0.000	0.000	0.032	0.000	0.000	0.082	0.000	0.143	0.000	0.068	0.000	0.036	0.000	0.074	0.096	0.029	0.000	0.001	0.000
Fe2+	0.485	0.524	0.509	0.520	0.515	0.485	0.522	0.476	0.522	0.433	0.509	0.492	0.547	0.490	0.463	0.485	0.465	0.518	0.541	0.521	0.537
Mn	0.012	0.010	0.010	0.011	0.012	0.011	0.012	0.013	0.012	0.011	0.012	0.011	0.012	0.012	0.010	0.012	0.011	0.011	0.011	0.011	0.011
Ni	0.000	0.000	0.000	0.000	0.000	0.000	0.000	0.000	0.000	0.000	0.000	0.000	0.000	0.000	0.000	0.000	0.000	0.000	0.000	0.000	0.000
Mg	1.910	1.805	1.786	1.770	1.848	1.695	1.867	1.916	1.822	2.009	1.768	1.919	1.851	1.857	1.615	1.899	1.915	1.875	1.842	1.830	1.828
Ca	0.560	0.604	0.660	0.665	0.612	0.711	0.611	0.577	0.617	0.518	0.631	0.561	0.572	0.641	0.728	0.579	0.595	0.606	0.601	0.640	0.598
Na	0.006	0.001	0.006	0.006	0.001	0.004	0.004	0.006	0.002	0.002	0.002	0.005	0.006	0.004	0.004	0.006	0.005	0.004	0.006	0.006	0.003
K	0.001	0.000	0.000	0.000	0.000	0.001	0.000	0.000	0.001	0.001	0.000	0.000	0.000	0.000	0.001	0.000	0.000	0.000	0.001	0.000	0.000
Total	8.000	8.000	8.000	8.000	8.000	8.000	8.000	8.000	8.000	8.000	8.000	8.000	8.000	8.000	8.000	8.000	8.000	8.000	8.000	8.000	8.000

	Garnet core (suite)																		
	L 117	L 118	L 119	L 129	L 130	L 131	L 133	L 136	L 139	L 140	L 141	L 143	L 144	L 145	L 146	L 147	L 149	Average	SD
SiO_2	41.11	42.58	41.64	42.04	41.94	42.10	41.81	42.50	42.77	42.76	42.59	42.23	42.56	42.21	42.21	42.44	42.46	**42.26**	**0.35**
TiO_2	0.11	0.13	0.13	0.10	0.10	0.13	0.12	0.09	0.13	0.16	0.13	0.11	0.13	0.16	0.14	0.11	0.14	**0.13**	**0.02**
Cr_2O_3	0.12	0.15	0.12	0.15	0.14	0.15	0.16	0.13	0.13	0.11	0.19	0.15	0.12	0.15	0.15	0.12	0.13	**0.14**	**0.02**
Al_2O_3	22.04	22.78	23.05	23.61	23.92	23.91	23.82	23.17	23.32	23.23	23.38	22.78	23.72	22.84	24.05	23.34	23.86	**23.39**	**0.50**
FeO	9.55	9.33	9.46	9.02	9.29	8.55	8.59	9.26	8.93	9.11	9.26	9.52	8.78	10.01	8.41	8.86	8.90	**8.99**	**0.45**
MnO	0.19	0.18	0.19	0.20	0.20	0.22	0.20	0.23	0.18	0.19	0.18	0.20	0.18	0.24	0.18	0.20	0.19	**0.19**	**0.02**
NiO	0.00	0.00	0.00	0.00	0.00	0.00	0.00	0.00	0.00	0.00	0.00	0.00	0.00	0.00	0.00	0.00	0.00	**0.00**	**0.00**
MgO	17.93	17.62	17.39	17.61	17.85	16.86	16.78	17.92	17.73	17.86	17.64	18.71	17.30	19.05	16.16	17.10	17.93	**17.39**	**0.74**
CaO	7.91	7.64	8.67	8.18	7.89	8.22	8.45	7.64	7.79	7.70	7.75	7.32	8.08	6.69	8.48	8.59	7.71	**8.02**	**0.57**
Na_2O	0.07	0.05	0.04	0.02	0.04	0.06	0.06	0.03	0.01	0.04	0.05	0.03	0.01	0.01	0.03	0.02	0.04	**0.04**	**0.02**
K_2O	0.01	0.01	0.00	0.00	0.01	0.00	0.00	0.01	0.00	0.00	0.00	0.00	0.00	0.00	0.00	0.00	0.00	**0.00**	**0.00**
Total	99.03	100.49	100.70	100.92	101.38	100.20	100.00	100.99	100.99	101.16	101.18	101.05	100.88	101.36	99.81	100.78	101.36	**100.55**	**0.58**
Numbers of ions on 12 Oxygen																			
Si	2.970	3.037	2.965	2.981	2.959	3.010	2.996	3.012	3.032	3.025	3.015	2.984	3.022	2.974	3.037	3.020	2.994	**3.010**	**0.026**
Ti	0.006	0.007	0.007	0.005	0.005	0.007	0.007	0.005	0.007	0.008	0.007	0.006	0.007	0.009	0.007	0.006	0.008	**0.007**	**0.001**
Cr	0.007	0.009	0.007	0.008	0.008	0.008	0.009	0.007	0.007	0.006	0.011	0.008	0.007	0.008	0.008	0.007	0.007	**0.008**	**0.001**
Al4	0.030	0.000	0.035	0.019	0.041	0.000	0.004	0.000	0.000	0.000	0.000	0.016	0.000	0.026	0.000	0.000	0.006	**0.007**	**0.011**
Al6	1.846	1.915	1.899	1.955	1.948	2.015	2.008	1.935	1.948	1.937	1.951	1.882	1.985	1.871	2.040	1.958	1.977	**1.958**	**0.050**
Fe3+	0.175	0.000	0.122	0.049	0.081	0.000	0.000	0.028	0.000	0.000	0.001	0.117	0.000	0.130	0.000	0.000	0.013	**0.031**	**0.048**
Fe2+	0.402	0.556	0.441	0.486	0.467	0.511	0.515	0.520	0.529	0.539	0.547	0.445	0.521	0.459	0.506	0.527	0.512	**0.505**	**0.035**
Mn	0.011	0.011	0.011	0.012	0.012	0.013	0.012	0.014	0.011	0.011	0.011	0.012	0.011	0.014	0.011	0.012	0.011	**0.011**	**0.001**
Ni	0.000	0.000	0.000	0.000	0.000	0.000	0.000	0.000	0.000	0.000	0.000	0.000	0.000	0.000	0.000	0.000	0.000	**0.000**	**0.000**
Mg	1.930	1.873	1.845	1.861	1.877	1.797	1.792	1.893	1.873	1.883	1.861	1.971	1.831	2.001	1.733	1.813	1.884	**1.846**	**0.071**
Ca	0.612	0.584	0.661	0.621	0.596	0.630	0.649	0.580	0.592	0.584	0.588	0.554	0.615	0.505	0.654	0.655	0.582	**0.612**	**0.046**
Na	0.009	0.007	0.006	0.003	0.005	0.008	0.008	0.004	0.001	0.005	0.007	0.004	0.002	0.002	0.005	0.003	0.006	**0.005**	**0.003**
K	0.001	0.001	0.000	0.000	0.001	0.000	0.000	0.001	0.000	0.000	0.000	0.000	0.000	0.000	0.000	0.000	0.000	**0.000**	**0.000**
Total	8.000	8.000	8.000	8.000	8.000	8.000	8.000	8.000	8.000	8.000	8.000	8.000	8.000	8.000	8.000	8.000	8.000	**8.000**	**0.000**

Table S2. Composition (in wt. %) of the minerals forming the reaction zone

Orthopyroxene

Sample	SiO_2	TiO_2	Al_2O_3	MgO	FeO	MnO	CaO	Na_2O	K_2O	Cr_2O_3	Total	Mg#
Opx_09	47.72	0.03	14.74	25.82	9.65	0.18	1.52	0.01	0.00	0.14	99.81	82.7
Opx_10	48.68	0.13	13.22	26.44	9.63	0.21	1.59	0.08	0.00	0.10	100.09	83.0
Opx_11	48.58	0.18	12.37	26.03	10.04	0.18	1.89	0.03	0.01	0.08	99.39	82.2
Opx_12	49.30	0.21	10.47	25.47	11.86	0.28	2.23	0.03	0.00	0.22	100.07	79.3
Opx_14	52.46	0.06	6.85	27.87	9.72	0.21	2.52	0.02	0.01	0.11	99.84	83.6
Opx_15	53.34	0.25	4.25	27.85	11.65	0.29	2.60	0.01	0.00	0.14	100.38	81.0
Opx_16	51.45	0.20	7.21	26.40	12.53	0.24	2.16	0.04	0.01	0.04	100.29	79.0
Opx_17	48.90	0.15	12.10	25.60	11.74	0.23	1.57	0.03	0.01	0.07	100.40	79.5
Opx_18	51.90	0.42	6.79	26.16	12.28	0.29	1.57	0.27	0.33	0.14	100.15	79.2
Opx_19	54.62	0.12	2.45	29.49	10.54	0.29	2.38	0.01	0.03	0.09	100.01	83.3
Opx_20	53.87	0.14	3.81	28.38	11.62	0.25	2.19	0.01	0.01	0.07	100.35	81.3
Opx_22	47.23	0.46	13.86	24.91	11.09	0.21	1.87	0.04	0.00	0.22	99.90	80.0

Olivine

Sample	SiO_2	TiO_2	Al_2O_3	MgO	FeO	MnO	CaO	Na_2O	Cr_2O_3	Total	Mg#
Oli_21	39.2	0.05	0.20	42.73	17.41	0.34	0.24	0.04	0.07	100.29	81.4
Oli_46	37.63	0.07	0.17	39.95	20.12	0.39	0.26	0.02	0.06	98.67	78.0

Spinel

Sample	SiO_2	TiO_2	Al_2O_3	MgO	FeO	MnO	CaO	Cr_2O_3	NiO	Total	Mg#	Cr#
Spi_1	0.13	0.05	66.61	20.88	11.77	0.09	0.03	0.50	0.02	100.07	76.0	0.50
Spi_2	0.10	0.05	66.49	20.67	11.92	0.11	0.03	0.48	0.06	99.91	75.6	0.48
Spi_3	0.14	0.04	66.60	20.54	11.91	0.09	0.05	0.59	0.03	99.99	75.5	0.59
Spi_4	0.17	0.03	66.69	20.71	11.87	0.12	0.04	0.65	0.05	100.33	75.7	0.65
Spi_5	0.10	0.00	66.66	20.84	11.86	0.13	0.03	0.53	0.03	100.19	75.8	0.53
Spi_10	0.32	0.13	64.18	19.15	15.18	0.14	0.13	0.59	0.01	99.84	69.2	0.61
Spi_11	0.11	0.01	66.19	20.31	12.40	0.12	0.06	0.43	0.01	99.64	74.5	0.43
Spi_12	0.20	0.11	64.79	19.33	15.10	0.11	0.06	0.49	0.00	100.19	69.5	0.50
Spi_29	0.29	0.07	66.08	20.79	12.26	0.11	0.08	0.41	0.01	100.10	75.1	0.41
Spi_30	0.34	0.17	64.03	19.24	15.24	0.10	0.16	0.72	0.03	100.02	69.2	0.75
Spi_31	0.29	0.14	64.32	19.19	15.52	0.15	0.13	0.58	0.02	100.34	68.8	0.60
Spi_32	0.23	0.09	65.61	20.93	12.42	0.09	0.09	0.60	0.05	100.12	75.0	0.61
Spi_33	0.16	0.06	65.85	20.49	13.04	0.12	0.10	0.39	0.06	100.27	73.7	0.39
Spi_34	0.14	0.07	66.03	20.81	12.57	0.11	0.10	0.46	0.02	100.30	74.7	0.47
Spi_36	2.21	0.16	62.74	18.94	15.16	0.16	0.49	0.69	0.01	100.56	69.0	0.73
Spi_37	0.34	0.08	64.29	18.97	15.11	0.14	0.13	0.48	0.07	99.62	69.1	0.50

Plagioclase

Sample	SiO_2	TiO_2	Al_2O_3	MgO	FeO	MnO	CaO	Na_2O	K_2O	Total	$An_{content}$
Plg_2	45.92	0.04	32.58	0.36	0.74	0.03	17.44	1.18	0.30	98.60	89.1
Plg_3	46.37	0.02	32.83	0.23	0.48	0.03	17.24	1.28	0.36	98.85	88.2
Plg_4	45.21	0.02	33.39	0.29	0.64	0.00	18.21	0.80	0.20	98.76	92.7
Plg_13	44.88	0.02	33.87	0.25	0.53	0.00	18.33	0.72	0.26	98.86	93.4
Plg_14	44.97	0.03	33.64	0.22	0.54	0.03	18.10	0.82	0.33	98.68	92.4
Plg_15	44.60	0.02	33.82	0.18	0.61	0.01	18.45	0.77	0.28	98.74	93.0
Plg_16	45.52	0.02	33.49	0.23	0.71	0.00	17.58	1.16	0.18	98.89	89.3
Plg_17	45.96	0.04	33.34	0.22	0.62	0.04	17.34	1.36	0.29	99.20	87.6
Plg_18	45.37	0.03	33.82	0.17	0.61	0.03	17.75	1.15	0.25	99.17	89.5
Plg_19	46.18	0.00	33.36	0.23	0.53	0.02	17.20	1.27	0.43	99.23	88.2
Plg_20	45.50	0.03	33.96	0.22	0.63	0.00	18.03	0.96	0.21	99.53	91.2
Plg_21	45.46	0.02	33.38	0.26	0.51	0.02	17.52	1.03	0.34	98.54	90.4
Plg_22	45.49	0.01	33.74	0.25	0.56	0.02	18.00	0.70	0.43	99.21	93.4
Plg_23	45.92	0.03	33.50	0.29	0.61	0.02	17.47	1.07	0.26	99.17	90.0
Plg_24	44.93	0.06	33.83	0.17	0.62	0.02	17.88	1.01	0.19	98.71	90.7
Plg_25	47.25	0.04	32.59	0.31	0.58	0.00	16.30	1.65	0.42	99.14	84.5
Plg_27	45.61	0.05	33.68	0.27	0.59	0.00	17.67	0.96	0.33	99.16	91.1
Plg_28	45.77	0.03	33.37	0.26	0.55	0.01	17.34	1.16	0.37	98.85	89.2
Plg_33	45.07	0.03	33.46	0.25	0.62	0.02	18.03	0.93	0.33	98.74	91.5
Plg_34	45.83	0.05	33.49	0.21	0.51	0.01	17.68	1.14	0.38	99.31	89.5
Plg_36	45.51	0.10	32.91	0.32	0.79	0.03	17.61	1.05	0.35	98.66	90.3
Plg_38	45.43	0.01	33.44	0.28	0.64	0.02	18.02	0.85	0.36	99.05	92.1

Table S3. Trace element content (in ppm) of *petit-spot* garnet xenocryst

n# analysis		**Grt 91**	**Grt 105**
Ba	ppm	1.47	1.90
Th	ppm	< b.d.l.*	0.002
U	ppm	0.002	0.002
Nb	ppm	0.013	0.009
Ta	ppm	< b.d.l.	< b.d.l.
La	ppm	0.003	0.01
Ce	ppm	0.041	0.064
Pb	ppm	0.011	0.036
Pr	ppm	0.025	0.028
Sr	ppm	2.80	1.37
Nd	ppm	0.39	0.44
Sm	ppm	0.39	0.41
Zr	ppm	8.51	8.80
Hf	ppm	0.21	0.23
Eu	ppm	0.29	0.28
Gd	ppm	0.71	0.72
Tb	ppm	0.13	0.14
Dy	ppm	1.02	0.94
Ho	ppm	0.21	0.20
Y	ppm	5.10	4.96
Er	ppm	0.61	0.52
Yb	ppm	0.66	0.60
Lu	ppm	0.087	0.088

*: <b.d.l. : below detection limit